



# Origin and tunability of dual color emission in highly stable Mn doped CsPbCl<sub>3</sub> nanocrystals grown by a solid-state process

Joydip Ghosh<sup>a</sup>, Modasser Hossain<sup>a</sup>, P.K. Giri<sup>a,b,\*</sup>

<sup>a</sup> Department of Physics, Indian Institute of Technology Guwahati, Guwahati 781039, India

<sup>b</sup> Centre for Nanotechnology, Indian Institute of Technology Guwahati, Guwahati 781039, India

## ARTICLE INFO

### Article history:

Received 1 November 2019

Received in revised form 12 December 2019

Accepted 16 December 2019

Available online xxx

### Keywords

Mn doped perovskite nanocrystals

Solid-state synthesis

Tunable dual-color emission

High stability

## ABSTRACT

Herein, we report on a facile, bulk scale room temperature solid-state synthesis of highly stable and luminescent Mn-doped CsPbCl<sub>3</sub> nanocrystal (NCs) with high Mn substitution, and investigate the origin and tunability of its dual-color emission. The structural and compositional analyses confirm the successful doping of Mn (1–40%) ion in CsPbCl<sub>3</sub> NCs. The Mn-doped CsPbCl<sub>3</sub> NCs exhibit distinct excitonic photoluminescence (PL) emission at ~412 nm ( $I_{\text{ex}}$ ) and Mn related emission at ~590 nm ( $I_{\text{Mn}}$ ) with high PL quantum yield (up to 35%). Our study reveals that the intensity ratio  $I_{\text{Mn}}/I_{\text{ex}}$  could be widely tuned by a factor of 64 and 23 by changing the Mn concentration and the measurement temperature, respectively. The stronger Mn emission at higher temperature is attributed to the higher rate of transfer of photoexcited carriers from the excitonic state of CsPbCl<sub>3</sub> host to Mn related state. Further, excitation intensity-dependent PL along with time-resolved PL studies revealed important insights into the origin and tunability of Mn related orange-red PL in the dual color emitting Mn-doped CsPbCl<sub>3</sub> NCs. The PL line shape analysis revealed additional PL peak in the range ~634–666 nm, which grows stronger with higher doping concentration and it is attributed, for the first time, to structural defects in the NCs. Remarkably, the Mn-doped CsPbCl<sub>3</sub> NCs synthesized by our method exhibit about 10 times higher storage stability than those reported earlier due to the high Mn doping efficiencies achieved due to the strain induced enhanced doping process. Finally, white light emitting diodes (LEDs) were fabricated by employing blue-emitting CsPbCl<sub>1.5</sub>Br<sub>1.5</sub> NCs, green-emitting CsPbBr<sub>3</sub> NCs and orange-red emitting 10% Mn-doped CsPbCl<sub>3</sub> NCs all grown by the same method. Our work demonstrates a low-cost synthesis strategy for high Mn doping in CsPbCl<sub>3</sub> NCs with superior ambient stability and highly tunable emission.

© 2019

## 1. Introduction

Inorganic halide perovskite materials are a promising class of semi-conductors which are being studied extensively as future optoelectronic materials [1–4]. All-inorganic perovskite with the structural formula of CsPbX<sub>3</sub> (X are the same single or mixed halides) quantum dot (QDs) and nanocrystals (NCs) have drawn tremendous research attention over the past few years with the advantages of high photoluminescence (PL) quantum yield (QY), high photostability and widely tunable spectral range and the extraordinary performances in LEDs, solar cells, photodetectors etc [2,4–9]. Unfortunately, the perovskite materials still have some shortcomings, such as poor stability and device performance in presence of oxygen and water molecules, and the toxicity of lead [10,11]. Lead-free perovskite QDs and NCs are also reported, though the Pb-free materials exhibit low PL QY and poor stability than the lead-based NCs and QDs [12].

On the other hand, the partial substitution of Pb<sup>2+</sup> in lead-based perovskite by other impurity ions, such as Mn, and other main group metal cations, transition metal cations, and rare earth (RE) metal cations are also explored to improve the optoelectronic properties of the perovskite NCs [13–19]. In particular, Mn doping of CsPbCl<sub>3</sub> has received much attention in order to reduce the toxic Pb content and improve the PL quantum yield [13]. Parobek et al. first reported the doping of Mn<sup>2+</sup> ions in CsPbCl<sub>3</sub> NCs by a high-temperature hot injection method [20]. Since the bond dissociation energy of Pb-Cl and Mn-Cl bonds are nearly similar, this permits the partial substitution of Pb in CsPbCl<sub>3</sub> NCs with Mn without much distortion in the crystal lattice structure [13]. These Mn-doped CsPbCl<sub>3</sub> NCs show dual-color emission. The sharp PL peak in the UV region is due to the band edge excitonic recombination of the host CsPbCl<sub>3</sub> NCs, while the orange-red PL is attributed to the energy transfer from excited states of CsPbCl<sub>3</sub> to Mn<sup>2+</sup> followed by radiative recombination from <sup>4</sup>T<sub>1</sub> state to <sup>6</sup>A<sub>1</sub> state of Mn [13,14,16,21]. Interestingly, the Mn doping in CsPbCl<sub>3</sub> effectively improve the structural stability and optical properties of perovskite, besides the partial substitution of toxic Pb [22].

The current synthesis strategies of Mn-doped CsPbCl<sub>3</sub> are mostly limited to tedious methods, which involve the use of toxic volatile or-

\* Corresponding author at: Department of Physics, Indian Institute of Technology Guwahati, Guwahati 781039, India.

E-mail address: [giri@iitg.ac.in](mailto:giri@iitg.ac.in) (P.K. Giri)

ganic solvents, inert gas atmosphere, and high reaction temperature. The most explored synthesis strategies for Mn-doped CsPbCl<sub>3</sub> NCs are hot injection and cation exchange methods, which involve complex time-consuming processes [15,22–24]. Synthesis of perovskite NCs in hot injection method involve more complex experimental procedures than the cation exchange method, and in cation exchange method the crystallinity of the as-grown NCs is relatively poor. In hot injection method, different polar solvents, organic surfactants/ligands are used which causes poor stability of NCs and escape of Mn ions from the host CsPbCl<sub>3</sub> NCs [24]. Doping with high concentration of Mn is quite challenging by conventional method, since the doped Mn atoms reside near the surface and easily escape from the host CsPbCl<sub>3</sub> NCs. However, a low cost, facile synthesis process for Mn-doped CsPbCl<sub>3</sub> NCs at room temperature and the complete solvent-free environment is still unexplored. Zhu et al. reported composition tunable perovskite QDs by ball milling [25]. However, to our knowledge, there is no report concerning the room temperature physical synthesis of Mn-doped CsPbCl<sub>3</sub> NCs with superior optical properties.

In this report, we have studied on a facile, low-cost solvent-free, bulk scale room temperature physical synthesis of highly luminescent Mn-doped CsPbCl<sub>3</sub> NCs with high Mn substitution through ball milling, for the first time. First, the raw reactants are milled for 2 hrs with the help of zirconia balls in a zirconia vial to avoid any contamination. Next, a small amount of surfactant (oleylamine) is added and milled for 1 hr, which results in dual color emitting Mn-doped CsPbCl<sub>3</sub> NCs exhibiting superior optical properties. We have characterized the undoped and Mn-doped NCs systematically by field emission transmission electron microscopy (FETEM), X-ray diffraction (XRD), X-Ray photoelectron spectroscopy (XPS), Uv-visible absorption, room temperature, and low-temperature PL, time-resolved PL (TRPL) analyses. The structural and compositional analyses by XRD and XPS, respectively, confirm the proper substitution of Pb by Mn ion in CsPbCl<sub>3</sub> NCs. Low-temperature PL and excitation intensity-dependent PL study reveals important insights into the origin of Mn related orange-red PL in the dual color emitting Mn-doped CsPbCl<sub>3</sub> NCs. Further, it is demonstrated that Mn-doped CsPbCl<sub>3</sub> NCs synthesized by physical milling method exhibit superior stability due to the high Mn doping efficiencies achieved through the nonequilibrium synthesis conditions during milling. Furthermore, white LED devices were constructed by employing blue-emitting CsPbCl<sub>1.5</sub>Br<sub>1.5</sub> NCs, green-emitting CsPbBr<sub>3</sub> NCs and orange-red emitting 10% Mn-doped CsPbCl<sub>3</sub> NCs composite films with Poly(methyl methacrylate) (PMMA). Implications of these results for a low-cost synthesis strategy for Mn-doped CsPbCl<sub>3</sub> NCs with superior ambient stability for white light-emitting application are discussed.

## 2. Experimental details

### 2.1. Materials

Cesium chloride (CsCl, >99.5%, Merck), cesium bromide (CsBr 99.999%, Sigma Aldrich) lead (II) chloride (PbCl<sub>2</sub>, 99.99%, Sigma Aldrich), lead(II) bromide (PbBr<sub>2</sub>, 99.999%, Sigma Aldrich), manganese (II) chloride tetra-hydrate (MnCl<sub>2</sub>·4H<sub>2</sub>O, >99%, Merck), Poly(methyl methacrylate) (PMMA) powder (Sigma Aldrich) oleylamine (OAM, >98%, Sigma Aldrich) and toluene (>99.0%, Merck) are used as the starting materials for the synthesis work. All the reagents are used as-received, without any further purification.

### 2.2. Physical synthesis of undoped and Mn-doped CsPbCl<sub>3</sub> NCs

Equivalent mole of CsCl (0.5 mM) and PbCl<sub>2</sub> (0.5 mM) were mixed together along with 40 g zirconia balls of diameter 5 mm in a zirconia vial of 50 ml volume (Retsch) under ambient condition and physically milled in a planetary ball mill (Retsch, Germany) at rotation speed of 500 rpm for 2 h. This results in a fine powder of CsPbCl<sub>3</sub>. For

the growth of CsPbCl<sub>3</sub> NCs, next 0.2 ml oleylamine (OAM) was added to the milling vial and the milling process was continued for another 1 h for the formation of surfactant-assisted NCs. Further, the synthesized product was dispersed in 20 ml of toluene. Next, the mixture was centrifuged for 10 min at 8000 rpm, and the precipitation was separated and discarded and the NCs were re-dispersed in toluene to obtain the final product. As-prepared NCs dispersion was used for further characterizations.

For the growth of Mn-doped CsPbCl<sub>3</sub> NCs, different amount of PbCl<sub>2</sub> was replaced by MnCl<sub>2</sub> depending upon the deserved Mn doping concentration. Typically, 0.5 mM CsCl, x mM MnCl<sub>2</sub> and (0.5-x) mM PbCl<sub>2</sub> were mixed and milled at 500 rpm for 2 h. For example, for 10% Mn-doped CsPbCl<sub>3</sub> NCs, 0.5 mM CsCl, 0.45 mM PbCl<sub>2</sub> and 0.05 mM MnCl<sub>2</sub> were used. For the synthesis of Mn-doped CsPbCl<sub>3</sub> NCs, we followed the same milling conditions as used for the growth of CsPbCl<sub>3</sub> NCs. The undoped (0%) and different Mn-doped (X%) NCs are termed as Mn0 and MnX, respectively.

### 2.3. Physical synthesis of CsPbBr<sub>3</sub> NCs and CsPbCl<sub>1.5</sub>Br<sub>1.5</sub> NCs

We further synthesized CsPbBr<sub>3</sub> and CsPbCl<sub>1.5</sub>Br<sub>1.5</sub> NCs, which were used as green and blue-emitting materials, respectively, for a white light-emitting device (WLED). CsPbBr<sub>3</sub> and CsPbCl<sub>1.5</sub>Br<sub>1.5</sub> NCs were synthesized by the same method we used for the growth of undoped and Mn-doped CsPbCl<sub>3</sub> NCs. For the growth of green light-emitting CsPbBr<sub>3</sub> NCs, equivalent moles of CsBr (0.5 mM) and PbBr<sub>2</sub> (0.5 mM) were mixed and milled by the two-step surfactant-assisted physical milling method with the identical conditions as used for the growth of Mn-doped CsPbCl<sub>3</sub> NCs. For the synthesis of green light-emitting CsPbCl<sub>1.5</sub>Br<sub>1.5</sub> NCs, PbCl<sub>2</sub>, PbBr<sub>2</sub>, CsCl and CsBr were used as starting precursor materials.

### 2.4. Preparation of the NCs-PMMA film and construction of WLED

PMMA powders (0.5 g) were mixed with 2 ml of different NCs (CsPbCl<sub>1.5</sub>Br<sub>1.5</sub>, CsPbBr<sub>3</sub> and 10% Mn-doped CsPbCl<sub>3</sub> NCs) dispersed in toluene. After complete dissolution of PMMA particles by ultrasonication, each of the solutions was drop cast on cleaned transparent quartz substrates and dried by vacuum heating (50 °C) to obtain the NCs-PMMA solid films. The light emissions from films were measured by placing the film on a UV LED chip of wavelength 396 nm. For the construction of white light LED, first CsPbCl<sub>1.5</sub>Br<sub>1.5</sub> NCs/PMMA solution was drop cast on a cleaned quartz substrate and then dried. Next CsPbCl<sub>1.5</sub>Br<sub>1.5</sub> NCs/PMMA and 10% Mn-doped CsPbCl<sub>3</sub> NCs/PMMA solutions were drop casted sequentially on top of the film. Finally, the film on quartz is placed on a UV-LED chip, which gives bright white light emission.

### 2.5. Characterization techniques

The morphology and structural properties of undoped and doped samples were analyzed using a FETEM (JEOL-2100F) operated at 200 kV. An energy dispersive x-ray (EDX) spectrometer equipped in FETEM instrument was used for the characterization of the elemental compositions. XRD (Rigaku RINT 2500 TRAX-III, Cu K $\alpha$  radiation) patterns were recorded for the determination of phase and structure of different samples. XPS measurements were carried out with a PHI X-Tool automated photoelectron spectrometer (PHI X-tool, ULVAC-PHI Inc.) using Al K $\alpha$  X-ray (1486.6 eV) with a beam current of 5 mA. UV-Vis absorption spectra were recorded using a commercial spectrophotometer (PerkinElmer, Lambda 950). A commercial fluorimeter (Horiba Jobin Yvon, Fluoromax-4) was used to record the room temperature steady-state PL spectra of different NCs samples using a Xe lamp excitation and a 360 nm diode laser (CNI Laser) excitation along with

pass filter. An integrating sphere (FM-SPHERE, Horiba) attached with the fluorimeter was used to measure the absolute PL quantum yield (PL QY) of different samples. Temperature-dependent (80–350 K) PL measurements were carried out using a liquid nitrogen-cooled optical cryostat (Optistat DNV, Oxford Instruments) attached to the above fluorimeter. Time-resolved PL (TRPL) measurements were carried out using a 375 nm pulsed laser excitation, with an instrument time response of < 50 ps (LifeSpecII, Edinburgh Instruments).

### 3. Results and discussions

#### 3.1. Synthesis strategy and doping of NCs by physical milling

Fig. S1 (supporting information) illustrates a schematic of the synthesis steps of dual-color emitting highly luminescent Mn-doped CsPbCl<sub>3</sub> NCs by the facile physical milling method. The most explored synthesis process for undoped and Mn-doped CsPbCl<sub>3</sub> perovskite NCs/QDs is hot injection method [13,26]. In this multistep tedious process to dissolve different raw reagents like Cs<sub>2</sub>CO<sub>3</sub>, CsOAc (cesium acetate), PbX<sub>2</sub> (X = Cl, Br, I) metal salts, either polar solvents such as DMF and DMSO, or organic surfactants/ligands like 1-octadecene (ODE), oleic acid (OA) are used by heating at high temperature [20]. Note that the final colloidal NCs can easily degrade in polar solutions. Thus the final product is precipitated, centrifuged and stored in a nonpolar organic solvent like toluene or hexane. However, there is expected to be some residue of polar solvents and organic surfactants/ligands which may degrade the NCs very fast. On the other hand, in the case of physical milling, no polar solvents or organic ligands are used. In our case, a little amount (0.2 ml) of oleylamine (OAM) is used. The high-speed mechanical mixing gives the required reaction energy in a similar way as heating or ultrasonication needed for the cocrystal formation. Kaupp et al. proposed a three-step reaction mechanism to explain the molecu-

lar solid reactivity [27,28]. First, raw reactants are diffused through a mobile phase similar to amorphous solid and chemical reaction is followed; second, nucleation and growth of the product phase occurred and finally, the product separated and unreacted reactant surface was exposed for further reaction cycles [28]. In our case, we have explored a two steps physical milling for the growth of undoped and Mn-doped CsPbCl<sub>3</sub> perovskite NCs. For the Mn-doped perovskite NCs, high Mn doping efficiencies were achieved through the pressure-mediated synthesis conditions in physical milling, resulting in enhanced PL emission related to Mn. The 1st milling phase for 2 hrs ensures the completion of reaction and doping, while 2nd phase of OMA assisted milling results in the cubic shaped NCs. Note that the very small amount of added OMA ligand plays an important role which functionalized the surface of the NCs exhibiting strong fluorescence with better stability [25]. It is well known that the ball milling process produce strain in the synthesized NCs. This strain may result in the lowering dopant energy and effective substitution of Pb by Mn with high Mn doping efficiency [29].

#### 3.2. Morphology and structural analysis

##### 3.2.1. FETEM analysis

Morphology of undoped and Mn-doped CsPbCl<sub>3</sub> NCs was studied using FETEM imaging. Fig. 1(a–d) shows the FETEM images of as-grown Mn0, Mn3, Mn5, and Mn10 samples, respectively. All the figures show the cubic shaped structure of CsPbCl<sub>3</sub> NCs. Note that the bare CsPbCl<sub>3</sub> NCs are perfectly cubic shaped as shown in Fig. 1(a) and this is consistent with the literature, while with increasing Mn doping concentration the NCs shape is partly distorted [13]. This may be due to some structural deformation with high Mn substitution. The inset in each figure shows the digital photographs depicting the emission colors of the corresponding samples under the illumination of 395 nm UV light.

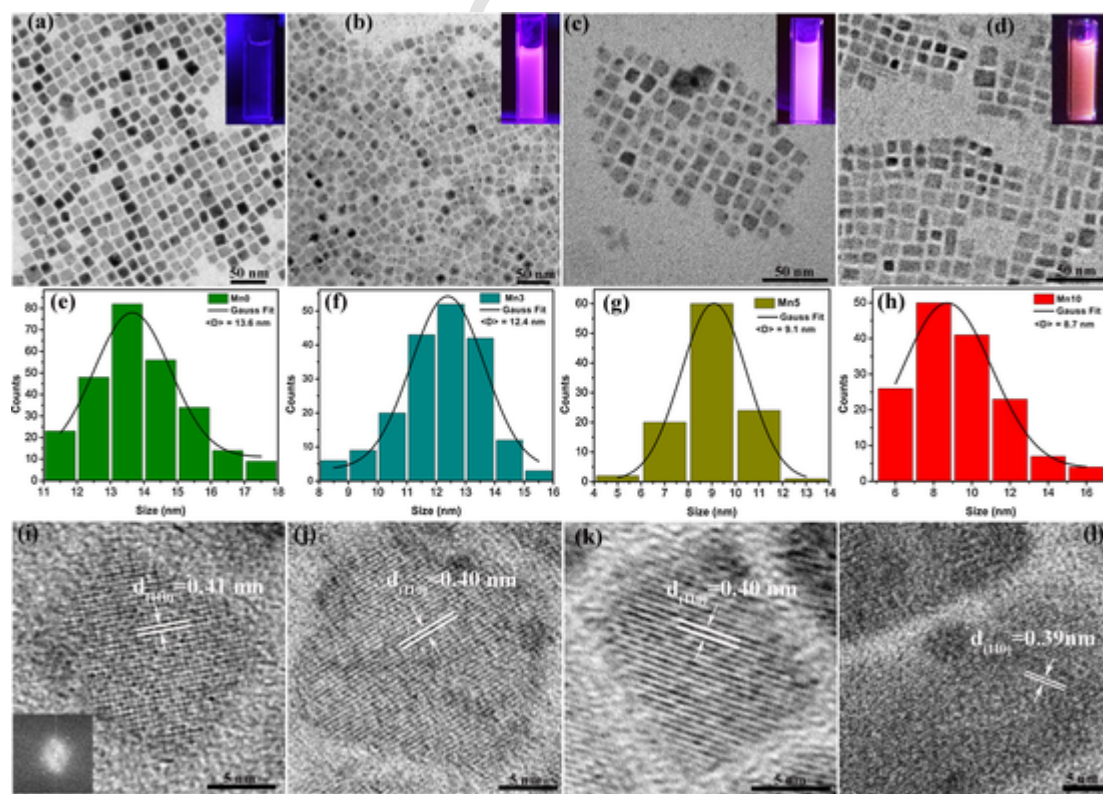


**Fig. 1.** TEM images of CsPbCl<sub>3</sub> NCs (a) undoped (b) 3% Mn-doped, (c) 5% Mn-doped, (d) 10% Mn-doped. Inset in each case shows the digital photograph depicting the emission colors of the corresponding samples under UV light irradiation. (e–h) Particle size distributions of undoped, 3%, 5% and 10% Mn-doped CsPbCl<sub>3</sub> NCs, respectively. The solid curve in each case shows the corresponding Gaussian fitting and (D) indicates the average size of the NCs. (i–l) The corresponding HRTEM lattice images of undoped, 3%, 5% and 10% Mn-doped CsPbCl<sub>3</sub> NCs, respectively. Inset of (i) shows the FFT pattern of CsPbCl<sub>3</sub> confirming its high crystalline quality.

Fig. 1(e–h) depicts the size distributions of NCs for different samples with corresponding Gaussian fitting. From the size distributions analysis, average sizes of the NCs were found to be 13.7, 12.4, 9.1 and 8.7 nm for Mn0, Mn3, Mn5, and Mn10, respectively. Interestingly, with the increase in Mn doping concentration, the average size of the NCs is decreased systematically [16,30]. This may be due to the partial substitution of  $\text{Pb}^{2+}$  ions ( $r = 0.133$  nm) by  $\text{Mn}^{2+}$  ions ( $r = 0.097$  nm) with smaller ionic radius. This decrease in NCs size with the increase in Mn doping concentration influences in the blue shift of band edge excitonic PL peak positions and absorption edges (discussed later). Fig. 1(i–l) shows the HRTEM lattice fringes of single NC of Mn0, Mn3, Mn5, and Mn10, respectively. The lattice spacing were found to be 0.41 nm, 0.40 nm, 0.40 nm and 0.39 nm for 0%, 3%, 5% and 10% Mn-doped  $\text{CsPbCl}_3$  NCs, respectively, which correspond to the (1 1 0) lattice plane of  $\text{CsPbCl}_3$ . It is clear that with the increase in Mn doping concentration, the lattice spacing decreased. Thus the gradual decrease in lattice spacing due to Mn doping corresponds to the substitution of bigger Pb atom by the smaller size Mn atom. These results are consistent with the XRD analysis (discussed later). The inset of Fig. 1(i) represents the corresponding fast Fourier transform (FFT) pattern of undoped  $\text{CsPbCl}_3$  NC, which confirms the good crystalline quality of the NC.

The elemental composition of Mn-doped  $\text{CsPbCl}_3$  NCs was further characterized by EDX analysis. Fig. S2 (supporting information) depicts the EDX elemental spectra of Mn3 which shows the presence of Cl, Cs, Pb, Mn with the atomic percentage of 57.7%, 18.4%, 21.2%, and 2.7%, respectively. This implied effective doping of Mn in the NCs. Effect of post-growth annealing on the morphology of doped NCs was studied by FESEM, as shown in Fig. S3(a) (supporting information). FESEM image of Mn10 film annealed at 100 °C for 30 min in Ar atmosphere shows the cubic shaped perovskite NCs. Some bigger size NCs were noticed, which may be due to agglomeration/grain growth during annealing. The corresponding spatial mapping for elements and EDX elemental spectra are shown in Fig. S3(b–e) and (f) (supporting information), respectively. The atomic percentage of different elements nearly matches with the percentage of parent raw materials confirming effective doping by this facile method.

### 3.2.2. XRD analysis

The crystalline quality and phase of undoped and Mn-doped  $\text{CsPbCl}_3$  NCs were studied by XRD analysis. Fig. 2(a) shows the comparison of XRD patterns of samples Mn0, Mn1, Mn3, Mn5, Mn10 and Mn20, respectively. The XRD pattern of undoped  $\text{CsPbCl}_3$  NCs confirms the desired cubic phase consistent with the literature [22,30]. The XRD patterns of Mn-doped  $\text{CsPbCl}_3$  NCs indicate that they retain the structures of the parent cubic  $\text{CsPbCl}_3$  NCs. Note that no impurity peak of raw reactants was observed in the XRD data profiles as shown in Fig. 2(a) confirming the proper reaction and full conversion of reactants in physical milling. Fig. 2(b) shows the magnified view of the XRD peak corresponding to (1 1 0) plane. Interestingly, with the increase in Mn doping concentration, the (1 1 0) peak is systematically shifted to higher angles with respect to that of undoped cubic  $\text{CsPbCl}_3$  NCs. For 20% Mn-doped NCs the shift is observed to be  $\sim 0.17^\circ$ . The systematic shift of the (1 1 0) peak toward higher angle is attributed to Mn incorporation in crystal and progressive lattice contraction due to the substitution of larger  $\text{Pb}^{2+}$  ions by the isovalent, yet smaller size,  $\text{Mn}^{2+}$  ions [22,30,31]. Note that a systematic decrease in lattice spacing with doping was also observed from HRTEM analysis. Thus, the result of XRD is fully consistent with the HRTEM analysis. We further calculated the compressive strain produced in the crystal structure of the doped NCs due to the Mn substitution from the shift of the XRD (1 1 0) peak and the results are shown in Table S1 (supporting information). For 20% Mn doping, the compressive strain is found to be 0.75%. Note that due to the high pressure mechanical milling, it naturally produces lattice strain in the crystal structure and it enhances the doping efficiency [29]. Zhu et al. showed that with 1% compressive strain (i) doping energy of Be in GaP is reduced by 0.2 eV and (ii) solubility of Be in GaP could be increased by 3 orders of magnitude at room temperature [29]. In the present work, we achieved  $\sim 40\%$  Mn doping in  $\text{CsPbCl}_3$  NCs, which is significantly higher than those reported in the literature.

### 3.2.3. XPS analysis

To investigate the chemical state, elemental composition, and doping, XPS analysis was performed on the as-grown undoped and 5% Mn-

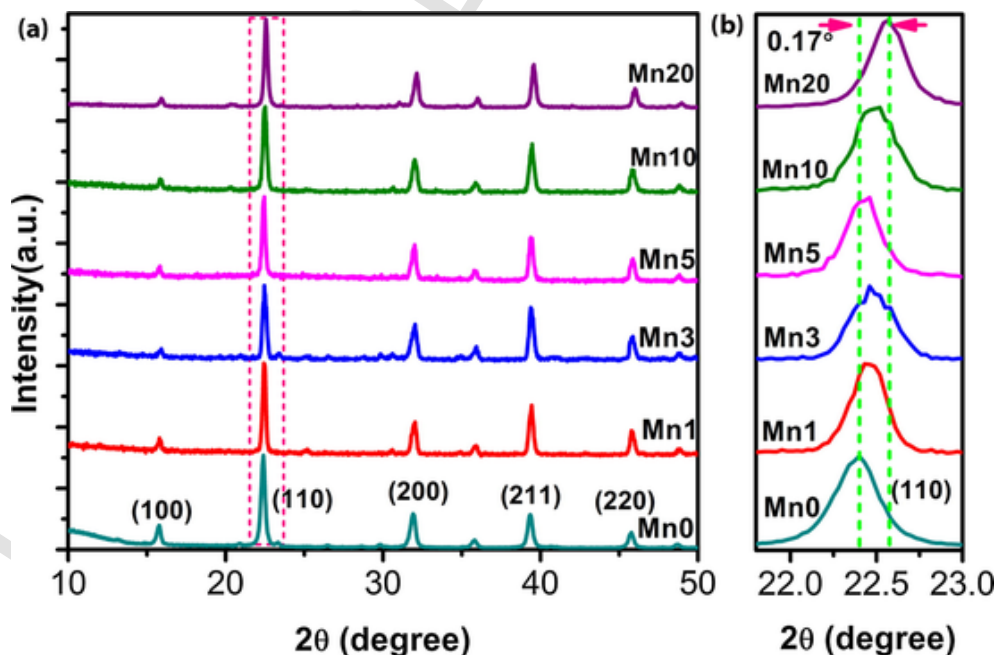


Fig. 2. (a) Comparison of the XRD pattern of samples Mn0, Mn1, Mn3, Mn5, Mn10, and Mn20. (b) A magnified view of the (1 1 0) peak of different samples, which show a systematic shift in peak position with doping concentration.

doped CsPbCl<sub>3</sub> NCs. Fig. 3(a) represents the survey scan XPS spectrum in the binding energy region 0–800 eV for Mn5. As shown in Fig. 3(a), the signals of Cs, Pb, Cl, Mn, C, and O are clearly observed [24,32]. Carbon and oxygen peaks with very low intensity were observed mainly due to the contamination/adsorption from the ambient air. Fig. 3(b) depicts the Mn 2p core-level XPS spectrum of Mn5 with the corresponding fitting. The peak with center at ~644.6 eV confirms the Mn<sup>2+</sup> state in the doped NCs [33]. Thus, XPS spectrum endorses the proper substitution of Pb ions by Mn ions in the Mn-doped CsPbCl<sub>3</sub> NCs. Fig. 3(c) shows the comparison of XPS peaks related to Cs in Mn0 and Mn5 with corresponding peak fittings. The peaks at 723.8 eV and 737.8 eV in undoped NCs correspond to Cs 3d<sub>5/2</sub> and 3d<sub>3/2</sub>, respectively, whereas for 5% Mn-doped NCs, Cs 3d<sub>5/2</sub> and 3d<sub>3/2</sub> peaks were observed at binding energy of 724.0 eV and 738.0 eV [33]. The peaks at ~138.0 eV and 143.0 eV for Mn0 represent Pb 4f<sub>7/2</sub> and 4f<sub>5/2</sub>, respectively, while for Mn5 the peaks were observed at ~138.2 eV and 143.1 eV [33]. The broad Cl 2p peak is fitted with two peaks (2p<sub>3/2</sub>, 2p<sub>1/2</sub>) with binding energies of 197.4 eV, 199.0 eV for Mn0 and 197.6 eV, 199.2 eV for Mn5, as shown 4(e). Interestingly, these

two closely spaced peaks of Cl may be attributed to the inner and surface Cl ions in the NCs.

### 3.3. Absorbance study

To investigate the doping effect in the optical band gap of undoped and Mn-doped CsPbCl<sub>3</sub> NCs, the absorption measurement was performed. Interestingly, with the increase in Mn doping concentration, the absorption edges of the doped samples are gradually blue shifted, as shown in Fig. 4(a). The blue shift may be attributed to the quantum confinement (QC) of carriers due to decrease in NCs size with high Mn substitution. However, since the NC sizes are much higher than the quantum confinement region (<5 nm), QC effect is unlikely to play any role in the observed blue shift. The excitonic PL emission is also blue-shifted due to Mn doping (discussed later). The contraction of the PbCl<sub>6</sub> octahedral unit and consequent enhancement of the interaction between Pb and Cl may also affect the blue shift of absorption edge [22]. We have further estimated the bandgap of each samples using the Tauc plot considering the direct bandgap nature of CsPbCl<sub>3</sub> per-

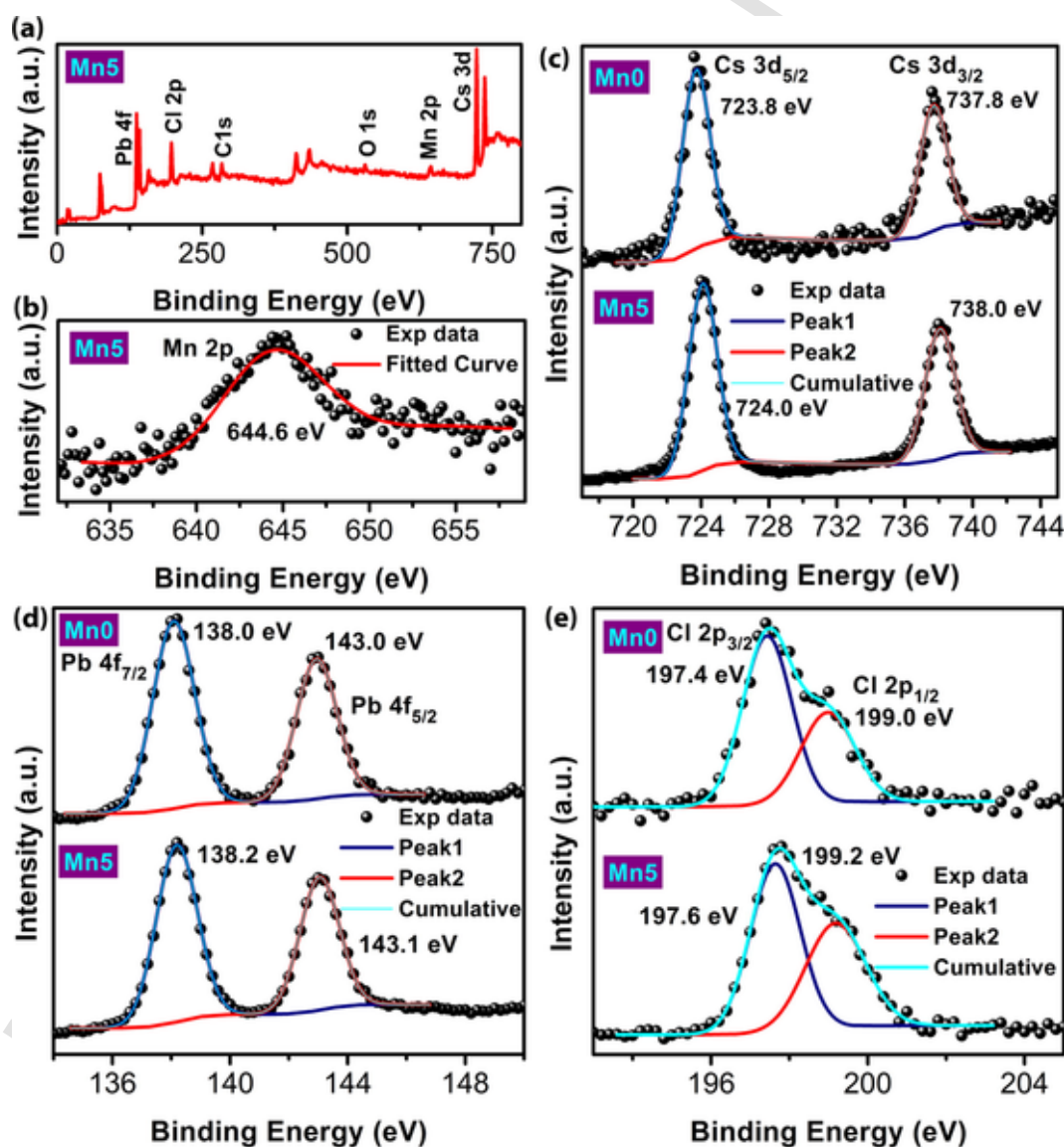


**Fig. 3.** (a) XPS survey scan spectrum in the binding energy range 0–800 eV of sample Mn5. (b) Mn 2p core-level spectrum of Mn5 with corresponding Gaussian fitting. (c) Comparison of Cs 3d core-level XPS spectra of Mn0 and Mn5 with Gaussian fittings. (d) Comparison of Pb 4f core-level XPS spectra of Mn0 and Mn5 with Gaussian fittings. (e) Comparison of Cl 2p core-level XPS spectra of Mn0 and Mn5 with fittings.

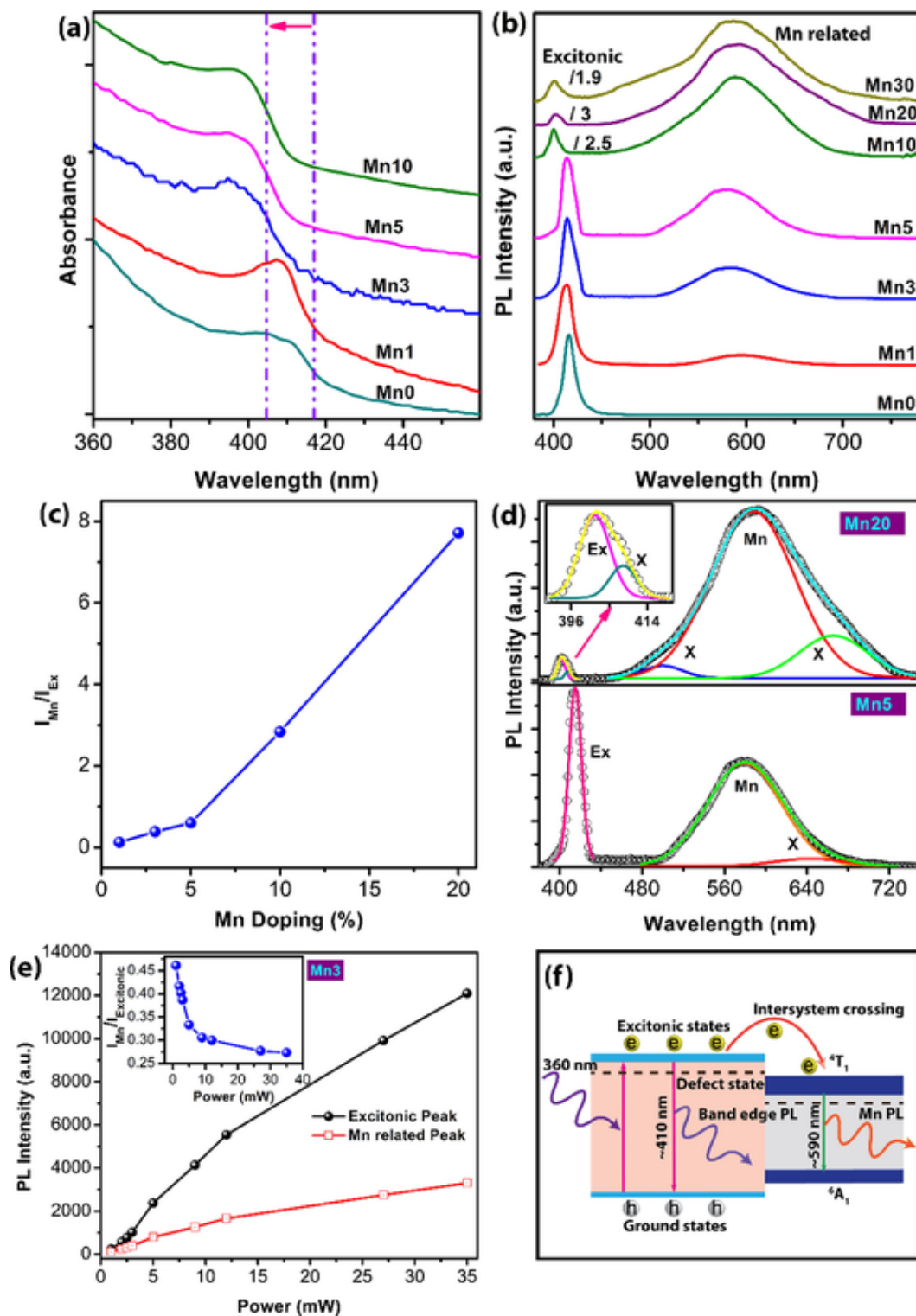


Fig. 4. (a) Comparison of absorbance spectra of Mn0, Mn1, Mn3, Mn5 and Mn10 showing a systematic blue shift in the absorption edge with increasing doping conc. (b) Comparison of PL spectra of undoped and Mn-doped (1–30%) CsPbCl<sub>3</sub> perovskite NCs. The plots for Mn10, Mn20 and Mn30 are scaled down by appropriate factors to enable comparison. (c) Change in the ratio of PL intensity of Mn related peak ( $I_{Mn}$ ) to that of the excitonic peak ( $I_{Excitonic}$ ) as a function of Mn concentration. (d) Deconvoluted PL spectra of Mn5 and Mn10 with corresponding Gaussian fittings. The inset shows a magnified view of the excitonic peak with fitting. (e) Change in PL intensity of Mn related peak and excitonic peak as a function of the excitation laser power. Inset shows the change in the intensity ratio  $I_{Mn}/I_{Excitonic}$  with excitation power. (f) Energy band diagram and PL emission mechanisms of CsPb<sub>2</sub>Mn<sub>1-x</sub>Cl<sub>3</sub> NCs. The horizontal dashed lines represent the defect-related energy levels.

ovskite [34]. From the Tauc plot (see Fig. S4, supporting information), bandgaps were found to be 2.94, 2.96, 2.96 and 3.01 eV for samples Mn0, Mn3, Mn5 and Mn10, respectively. Thus, the bandgap was found to increase with the increase in Mn doping concentration.

### 3.4. Photoluminescence study

The light-emitting property of undoped and Mn-doped CsPbCl<sub>3</sub> NCs was investigated by the PL measurements. Fig. 4(b) shows the PL spectra of undoped and Mn-doped CsPbCl<sub>3</sub> NCs with different Mn concentration under 360 nm excitation. The PL peak at ~416 nm with narrow FWHM for undoped CsPbCl<sub>3</sub> NCs corresponds to the band to band excitonic recombination of photogenerated carriers. The Mn-doped CsPbCl<sub>3</sub> samples show dual-color emission with a broad emission in the orange-red region with a peak at ~590 nm besides the excitonic emission in the UV region. The emission in the region ~460–720 nm is attributed to Mn related emission. This orange-red emission originates from the energy transfer of photoexcited excitons from the excited states of the CsPbCl<sub>3</sub> host to the doped Mn<sup>2+</sup> states facilitating recombination of excitons via a radiative pathway in the states of Mn [13,20]. Thus, the PL spectra of Mn-doped CsPbCl<sub>3</sub> NCs further confirm the successful incorporation of Mn<sup>2+</sup> ions into CsPbCl<sub>3</sub> NCs. The XRD and XPS analysis also confirm the substitution of Pb<sup>2+</sup> ions by Mn<sup>2+</sup> ions. In this work, we demonstrate the CsPb<sub>x</sub>Mn<sub>1-x</sub>Cl<sub>3</sub> perovskite NCs with a Mn substitution ratio up to 20% by physical milling, which is comparable/higher than the reported doping concentration of Mn in CsPbCl<sub>3</sub> [18,22]. As shown in Fig. 4(b), with the increase in Mn doping content from 0% to 20%, the relative intensity of the Mn related emission is increased systematically with respect to the intensity of the excitonic PL emission. This is due to the higher transfer of photogenerated excitons to the Mn<sup>2+</sup> state in the samples with a higher content of Mn substitution. The change in the ratio of Mn PL to excitonic PL peak intensity with Mn doping content is shown in Fig. 4(c), which shows nearly a linear increase in PL intensity with doping concentration [35]. Note that the actual Mn content in the NCs may be lower than the actual amount used for the synthesis. EDX spectra reveal the Mn concentration as 2.7%, 8.6% and 13.4% Mn for corresponding doping of 3%, 10% and 20%, respectively. On the other hand, XPS analysis revealed higher content of Mn in each sample due to its high concentration expected near the surface of the NCs, as XPS probes only ~10 nm depth from the surface. Note that beyond 20% doping, the overall PL quantum yield is reduced, which may be due to the nonradiative defects and deformation of the crystal structure in the NCs, as shown in Table 1 and Fig. S6(a) (supporting information).

For a better comparison of Mn related emission, each spectrum is normalized to the corresponding band edge excitonic emission. The normalized PL spectra of undoped and Mn-doped CsPbCl<sub>3</sub> perovskite NCs are shown in figure S5(a) (supporting information). The PL emission spectrum of each sample shows dual emission peaks centered at ~406 and ~590 nm, respectively. The band-edge emission peak is narrow with the full width at half-maximum (FWHM) of ~11–16

nm and it is assigned to the excitonic emission of the CsPbCl<sub>3</sub> host, whereas the 590 nm peak is broad with the FWHM of ~75–120 nm, which is due to the doped Mn<sup>2+</sup> ions in CsPbCl<sub>3</sub> NCs. The orange-red PL band with a larger FWHM and homogenous broadening originates due to the existence of a continuous set of vibrational sublevels in each electronic states related to Mn<sup>2+</sup> [13]. The systematic increase in FWHM of Mn related PL peak with the increase in Mn doping concentration is shown in Fig. S5(b) (supporting information) which further supports our claim on the origin of broad Mn PL emission. Inset of Fig. S5(a) (supporting information) shows the shift of excitonic PL emission peaks of different samples. Interestingly, with the increase in Mn doping concentration from 0% to 20%, the band edge excitonic peaks are blue-shifted from 416 nm to 402 nm. This is consistent with the blue shift of the absorption spectra. Since the NCs sizes are much higher than the excitonic Bohr radius, quantum confinement effect is unlikely to play any role in the blue shift of PL peak. The blue shift of the excitonic PL and band edge may be due to the contraction of the PbCl<sub>6</sub> octahedral unit and consequent enhancement of the interaction between Pb and Cl [22]. However, excess Mn substitution (>20%) may distort the lattice heavily and eventually destroy the crystallinity with increasing structural defects in the host, which reduces the PL QY as shown in S6(a) [13].

The PL quantum yields were measured to be 11%, 19%, 24%, 32%, 36%, 26% for samples Mn0, Mn1, Mn3, Mn5, Mn10 and Mn20, respectively. Note that with doping of a small amount of Mn (1%), the overall PL QY was increased from 11% to 19%. The low PL QY (11%) of the undoped sample is attributed to the mid-bandgap trap states that facilitate nonradiative recombination in wide bandgap CsPbCl<sub>3</sub> NCs [22]. The large increase in excitonic band edge PL intensity with 1% Mn doping is possibly due to the removal of pre-existing structural defects in the host CsPbCl<sub>3</sub> NCs due to the doping [22]. With the increase in Mn doping content, PL QY is systematically increased up to 35% for 10% Mn doping, while it is decreased to 26% for 20% doping. This may be due to a decrease in crystallinity and structural defects of the NCs with a high content of Mn substitution. The details of excitonic PL and Mn related PL and PL QY of different samples are summarized in Table 1.

Since the physical milling is a non-equilibrium process, structural defects are likely to be introduced during the physical milling process. To analyze the defect-related emission due to high Mn substitution, we have deconvoluted the excitonic and Mn related PL peaks of Mn5 and Mn20, as shown in Fig. 4(d). For Mn5, the excitonic PL peak was fitted with one Gaussian peak (excitonic), while the Mn related peak was deconvoluted with two Gaussian peaks (Mn related and X). However, for Mn20, the excitonic PL peak was fitted with two Gaussian peaks (excitonic and X), while the Mn related peak was deconvoluted with three Gaussian peaks (Mn related and X). The peak X observed in Mn20 with higher weightage than that of Mn5 is due to the radiative recombination from the sub-bandgap defect states in Mn20. We propose that the X corresponds to the radiative recombination due to the defect-related sub-bandgap states originating from the ball milling process. It is clear that with the increase in Mn doping content, the sub-bandgap defect states (X band) increased since high doping density leads to a higher amount of disorder in the crystal lattice and creates more defect states. The details of the defect related X bands are summarized in Table 1. Further the PL peaks of 30% and 40% Mn doped CsPbCl<sub>3</sub> NCs were deconvoluted, as shown in Fig. S6(b) (supporting information). It is evident that the contribution of defect related peaks increased significantly for Mn30 and Mn40.

Note that there may be the presence of nonradiative decay pathways in the doped NCs due to room temperature synthesis process which results in the lower PL QY. To eliminate the structural defects, we have annealed the Mn5 sample at different temperatures for 20 min in Ar environment and studied the improvement in the structural

**Table 1**  
Summary of PL peak positions, relative intensity and PL quantum yields of different Mn doped CsPbCl<sub>3</sub> NCs.

Sample code	Excitonic PL peak (nm)	Mn related peak (nm)	Defect induced X bands (nm)	Intensity ratio I <sub>Mn</sub> /I <sub>Ex</sub>	PL quantum yield (%)
Mn0	416	–	–	–	11
Mn1	414	585	–	0.13	19
Mn3	414	581	634	0.39	24
Mn5	414	579	643	0.60	32
Mn10	400	591	526, 647	2.80	35
Mn20	402	588	500, 666	7.70	26
Mn30	401	589	505, 643	3.99	14
Mn40	398	592	504, 647	0.97	5

and optical properties. Fig. S7(a) (supporting information) shows the XRD spectra of Mn5 film annealed at different temperatures. Interestingly, the FWHM of (1 1 0) XRD peak systematically decreases with the increase in annealing temperature, which is may be due to improved crystallinity of the NCs caused by the annealing. Note that the absorbance of annealed films also increased with annealing temperature, as shown in Fig. S7(b) (supporting information). Thus the annealing results in the improved optical properties of the perovskite NCs film. The PL intensity was increased with the increase in annealing temperature up to 100 °C, which confirms the increase in crystallinity and reduction of nonradiative decay centers in the NCs, as shown in Fig. S7(c) (supporting information). We have deconvoluted the PL peaks of as-grown Mn5 (NCs dispersed in toluene) and annealed Mn5 (100 °C), as shown in Fig. S7(d) (supporting information). Along with the excitonic peak (peak1) and Mn related broad peak (peak2), a third peak (peak3) is observed for Mn5, which is attributed to sub-bandgap defect-related emission, which almost vanishes with annealing. Thus, the annealing of the samples improves the structural properties of the samples and yields higher PL QY.

For optimizing the milling time dependence of doping, we varied the duration of physical milling from 0.5 hr to 4 hrs. Interestingly, the Mn related PL intensity increases with the duration of milling up to 2 hrs for 5% Mn-doped CsPbCl<sub>3</sub> NCs (see Fig. S8, supporting information). No further increase of Mn PL was observed for sample milled up to 4 hrs. Thus, 2hrs of milling was chosen as the optimum for substitution of Pb by Mn ions.

The excitation intensity dependence of transfer of photogenerated excitons to Mn<sup>2+</sup> state was further studied to look for the color tenability of emission. Laser light of 360 nm with incident power 1 mW to 35 mW was used for the excitation. With the increase in excitation intensity, both the band edge emission and Mn related PL peaks increase in 3% Mn-doped NCs, though the increase in Mn PL is lower than that of the excitonic PL intensity. Fig. 4(e) depicts the comparison of the PL intensity of excitonic peaks and Mn related peaks with incident laser power. Both the peak intensity was increased with the increase in incident laser power as expected. However, the enhancement of the excitonic peak in the UV region is much higher than that of the orange-red peak. Inset of Fig. 4(e) shows the variation of ratio of Mn related PL to band edge excitonic emission ( $I_{Mn}/I_{Excitonic}$ ) with laser power. When Mn-doped CsPbCl<sub>3</sub> NCs was excited by light of wavelength 360 nm, electron-hole pairs (excitons) are created and confined inside the NCs. These photogenerated excitons can be deactivated mainly via three pathways: (a) radiative recombination through the band edge, (b) non-radiative recombination, (c) energy transfer to Mn<sup>2+</sup> ions and radiative relaxation from <sup>4</sup>T<sub>1</sub> state to <sup>6</sup>A<sub>1</sub> state. When the excitation fluence is in the weak excitation regime (that is, less than one photon per NC)  $I_{Excitonic}/I_{Mn}$  should be independent of excitation intensity. Note that the PL lifetime of Mn related state is of the order of milliseconds (ms), while the lifetime of excitonic emission is of the order of nanoseconds (ns) (discussed later). Thus, the Mn-doped CsPbCl<sub>3</sub> NCs can be additionally excited when the Mn<sup>2+</sup> ions are already in excited states with sufficient high excitation fluence, which results in the high excitonic PL intensity [26,36]. Thus  $I_{Excitonic}/I_{Mn}$  can be dependent on excitation intensity in the strong excitation regime. When nearly all Mn<sup>2+</sup> are in the <sup>4</sup>T<sub>1</sub> state, the Mn<sup>2+</sup> PL nearly saturates with the increase of excitation intensity. This excitation intensity-dependent control of the relative intensity of dual emission is an important phenomenon useful for light intensity driven color-tunable luminescence properties. Chen et al. reported excitation intensity-dependent color-tunable dual emissions from Mn-doped CdS/ZnS core/shell NCs [36]. Thus, Mn-doped CsPbCl<sub>3</sub> NCs can be also useful for excitation intensity-dependent color-tunable dual emissions. At low excitation, both the colors have comparable intensity, while at high excitation power, the UV emission dominates over the orange emission.

Based on the aforementioned results, the emission model of CsPb<sub>x</sub>Mn<sub>1-x</sub>Cl<sub>3</sub> NCs is illustrated through energy band diagram in Fig. 4(f) [13,17]. Excited by 360 nm light irradiation, the CsPbCl<sub>3</sub> host absorbs the photons and emits ~410 nm via the radiative recombination of excitons between the ground state and the excited state of CsPbCl<sub>3</sub>. Besides the radiative recombination, a nonradiative relaxation process also exists, which leads to energy loss through-hole traps or electron traps resulting in low PL QY of the undoped sample. The Mn doping in CsPbCl<sub>3</sub> NCs generates a new recombination pathway of excitons via the energy transfer from the excited state of host CsPbCl<sub>3</sub> to Mn<sup>2+</sup> and radiative recombination, which generates orange-red emission, as shown in Fig. 4(f) [13,22,37]. Only the excitons retaining enough thermal activation energy facilitate an intersystem crossing (ISC) process and finally emit around 590 nm emission, showing a new excitons recombination pathway. This well-known recombination pathway of this d-d transition of Mn<sup>2+</sup> ions is termed <sup>4</sup>T<sub>1</sub>-<sup>6</sup>A<sub>1</sub> transition [13,38]. In case of high doping concentration, defect-related emissions are observed, as denoted by the dashed lines in the band diagram.

### 3.5. Temperature-dependent photoluminescence study

To investigate the origin of dual-color emissions in Mn-doped CsPbCl<sub>3</sub> NCs, we further performed the low-temperature PL measurements at different temperatures. Fig. 5(a) shows the PL spectra of 3% Mn-doped CsPbCl<sub>3</sub> NCs, in the temperature range 80–350 K. The PL spectra at different temperatures are scaled approximately to enable better comparison. Note that the temperature-dependent PL measurement was performed on a film of the NCs deposited on a silicon substrate. Fig. 5(a) clearly shows that with the decrease in temperatures the near band edge PL peak intensity increases systematically. The increase in PL intensity with decreasing temperature is very common in semiconductors, which is mainly due to reduced carrier trapping and lower thermal quenching of PL at lower temperatures [39]. At higher temperature, the nonradiative recombination channels are more active and excitons may be dissociated, which results in the decrease the in PL intensity. Fig. 5(b) depicts the comparison of excitonic and Mn related PL peak intensity at different temperatures. Interestingly, the Mn emission peak intensity decreases gradually with the decrease in temperature from 350 K to 80 K. The unusual temperature dependence of Mn<sup>2+</sup> PL peak can be explained by the competitive recombination between the near band edge and <sup>4</sup>T<sub>1</sub> state to <sup>6</sup>A<sub>1</sub> state in Mn<sup>2+</sup> after energy transfer from host CsPbCl<sub>3</sub> [16]. When we increase the temperature from 80 K to 350 K, the photoexcited carriers located at the excitonic state of CsPbCl<sub>3</sub> get extra thermal energy ( $k_B T$ ) to dissociate and transit directly in <sup>4</sup>T<sub>1</sub> state in Mn<sup>2+</sup> ions. Thus the enhanced radiative recombination from <sup>4</sup>T<sub>1</sub> state to <sup>6</sup>A<sub>1</sub> state results in the higher intensity of Mn PL [16]. Thus, the Mn related state shows negative thermal quenching behavior. At low temperature, the more rapid excitonic recombination than the energy transfer to Mn<sup>2+</sup> state is responsible for the low-intensity Mn PL as compared to the high band edge emission, as shown in Fig. 5(a). With the increase in temperature, the excitons dissociate and the excitonic recombination slows down and the energy transfer to the Mn<sup>2+</sup> becomes more dominant, which results in the greater intensity of Mn PL at 350 K. The variation of excitonic PL intensity and Mn PL intensity with temperatures are shown in Fig. 5(b). From Fig. 5(a), it is clear that with the decrease in temperature, the Mn PL peak is partly quenched and red-shifted. The redshift of Mn PL peak with decreasing temperature is attributed to the decrease in crystal-field strength produced by thermal expansion of the host lattice and the thermal activation of vibronic hot bands [16]. This type of redshift is also observed in Mn-doped ZnS and ZnSe NCs [40]. Fig. 5(c) shows the deconvoluted PL spectra related to Mn at temperature 80 K and 350 K. The decrease of weightage of the PL peak at higher wavelength at 350 K reveals its nonradiative nature.

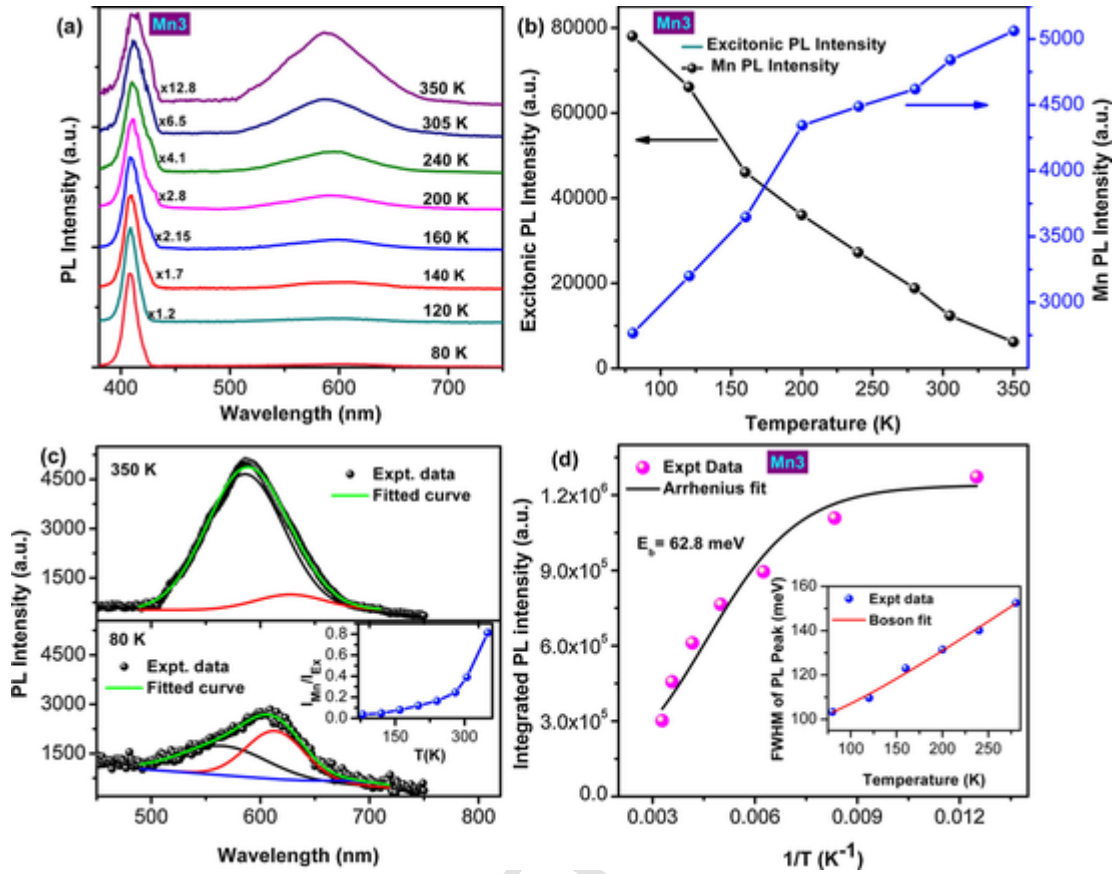


Fig. 5. (a) Temperature-dependent PL spectra of 3% Mn-doped CsPbCl<sub>3</sub> NCs film, PL spectra at different temperatures are scaled up appropriately to enable better comparison. (b) The evolution of excitonic PL intensity (left Y-axis) and Mn related PL intensity (right Y-axis) with temperature for Mn3. (c) Deconvoluted PL spectra of Mn related peak at temperatures 80 K and 350 K. (d) Variation of integrated PL intensity of excitonic peak with the inverse of temperature and its fitting with Arrhenius equation. The inset shows the variation of FWHM of the excitonic peak with temperatures and its Boson fit.

From the low-temperature PL spectra, we can also estimate two important parameters: (a) exciton binding energy ( $E_b$ ) and (b) exciton-phonon scattering coefficient [39]. Thus, we calculated the exciton binding energy of 3% Mn-doped CsPbCl<sub>3</sub> NCs from the temperature-dependent integrated PL intensity of the excitonic peak using the Arrhenius equation:

$$I(T) = \frac{I_0}{1 + A \exp(-E_b/k_b T)} \quad (1)$$

where  $I_0$  is the integrated PL intensity at very low temperature,  $E_b$  is the exciton binding energy,  $k_b$  is the Boltzmann constant, A is constant. Fig. 5(d) shows the variation of integrated PL intensity of excitonic peak with the inverse of temperature ( $1/T$ ) fitted with the Arrhenius equation. The obtained  $E_b$  is 62.8 meV [5]. Note that the low-temperature PL measurement was performed on a film of the NCs deposited on silicon substrates, where the spontaneous aggregation of the NCs may partly quench the PL intensity. Thus the actual exciton binding energy in individual NCs may be higher than the above-calculated value. This low exciton binding energy is consistent with the decrease in excitonic emission and an increase in Mn related emission at higher temperatures.

The inset of Fig. 5(d) depicts the variation of FWHM of excitonic PL peak with temperatures. It is clear from Fig. 5(d) that the FWHM of PL peaks is increased with increasing temperature. The higher broadening with the increase in temperature is due to the enhanced exciton-phonon scattering and non-radiative decay of photogenerated excitons in perovskite NCs [39]. The PL peak broadening  $\Gamma$  is fitted using the Boson model with the following equation [41,42]

$$\Gamma(T) = \Gamma_0 + \sigma T + \frac{\Gamma_{op}}{\exp(E_{ph}/k_b T) - 1} \quad (2)$$

where  $\Gamma_0$  is the inhomogeneous broadening constant due to exciton-exciton scattering and  $\sigma$  is the exciton-acoustic phonon coupling coefficient.  $\Gamma_{op}$  corresponds to the exciton-longitudinal optical phonon coupling coefficient or the Fröhlich coupling coefficient, whereas  $E_{ph}$  is the optical phonon energy. From the fitted data, the obtained parameters are as follows:  $\Gamma_0 = 91.9$  meV,  $\sigma = 127.6$   $\mu\text{eV/K}$ ,  $\Gamma_{op} = 47.9$  meV, and  $E_{ph} = 26.1$  meV. These parameters indicate strong exciton-phonon interactions in the doped CsPbCl<sub>3</sub> NCs and it leads to broadening of excitonic PL peak as the temperature is increased from 80 to 350 K [42]. The obtained parameter are consistent with the reported value of optical phonon energy using Raman scattering experiment for CsPbCl<sub>3</sub>, which showed a  $E_{ph}$  of 27.6 meV [43].

### 3.6. Time-resolved photoluminescence study

To investigate the recombination kinetics of photogenerated charge carriers, TRPL measurements were performed on the undoped and Mn-doped CsPbCl<sub>3</sub> NCs with 375 nm laser excitation. Fig. 6(a) shows the comparison of TRPL decay profiles of Mn0, Mn3, Mn5, and Mn10 monitored at respective excitonic peaks. Each of the TRPL decay profile was fitted using a tri-exponential decay function as:

$$A(t) = \sum_{i=1}^{i=3} A_i \exp\left(-\frac{t}{\tau_i}\right) \quad (3)$$

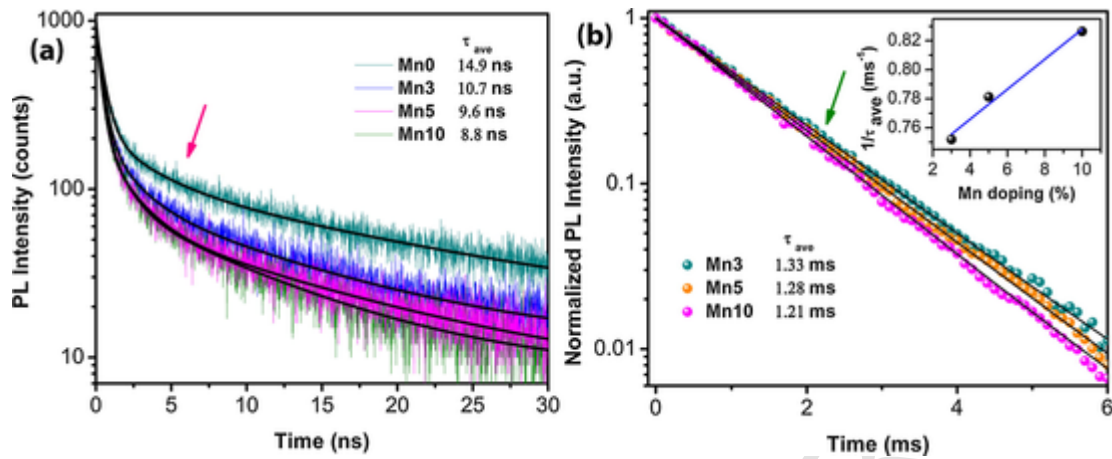


Fig. 6. (a) TRPL decay profiles of Mn0, Mn3, Mn5, Mn10 with tri-exponential fitting corresponding to the excitonic PL peak. (b) TRPL decay profiles of Mn3, Mn5, Mn10 with single exponential fit corresponding to the Mn related PL peak. The inset shows the  $1/\tau_{ave}$  vs. Mn doping concentration with a linear fit.

where  $A_i$  is the amplitude with lifetime  $\tau_i$ . The average lifetime ( $\tau_{ave}$ ) of decay was estimated using the relation.

$$\tau_{ave} = \frac{\sum_{i=1}^3 A_i \tau_i^2}{\sum_{i=1}^3 A_i} \quad (4)$$

The details of the carrier lifetimes ( $\tau_i$ ) and amplitudes ( $A_i$ ) for undoped and different Mn-doped samples are tabulated in Table S2 (supporting information). The average lifetimes of the excitonic PL peak were obtained to be 14.9, 10.7, 9.6, 8.8 ns for Mn0, Mn3, Mn5, and Mn10, respectively. Thus the average lifetimes decreased systematically with the increase in Mn doping concentration. This may be due to the decrease in NCs size and quantum confinement effect with the increase in Mn substitution content [39]. Note that due to the Mn doping, parts of the free carriers are transferred to the Mn ions and this may effectively shorten the excitonic carrier lifetime. At room temperature, this effect is prominent. However, at low temperature, this effect is less prominent and giving rise to high excitonic PL intensity.

Fig. 6(b) shows the TRPL decay profiles of Mn related emission in Mn3, Mn5, and Mn10. For Mn emission, TRPL data profiles were fitted using single exponential decay function and the lifetimes were found to be 1.33 ms, 1.28 ms and 1.21 ms for Mn3, Mn5, and Mn10, respec-

tively. The long lifetime ( $\sim$ ms) of Mn PL is attributed to the spin-forbidden nature of the transition from  $^4T_1$  state to  $^6A_1$  state [16]. The decrease in the lifetime with increasing Mn content may be due to the enhanced Mn-Mn interaction [16]. Further, the carrier lifetime is expected to be inversely proportional to the impurity density,  $N_t$ , according to Shockley-Read-Hall (S-R-H) recombination theory [44]. Inset of Fig. 6(b) shows the variation of the inverse of decay constants with Mn doping concentration with linear fitting. Thus, these results are consistent with S-R-H theory.

### 3.7. Stability study

We have further studied the long-term stability of our 3% Mn-doped CsPbCl<sub>3</sub> NCs by PL measurements at certain time intervals. Fig. 7(a) shows the evolution of the PL spectra (normalized to the excitonic emission) after storing in ambient air (with high humidity) for time duration up to 75 days after synthesis. The variation of Mn PL peak intensity with storage times is shown in the inset of Fig. 7(a) which depicts the gradual decrease of PL intensity related to Mn with the increase in storage time. Note that the most explored synthesis method for CsPbCl<sub>3</sub> and Mn-doped CsPbCl<sub>3</sub> NCs is hot injection method. In this method, the stability of CsPb<sub>x</sub>Mn<sub>1-x</sub>Cl<sub>3</sub> NCs is of main concern, as Mn<sup>2+</sup> ions gradually escape from the host CsPbCl<sub>3</sub> with storage time [18,45]. In the

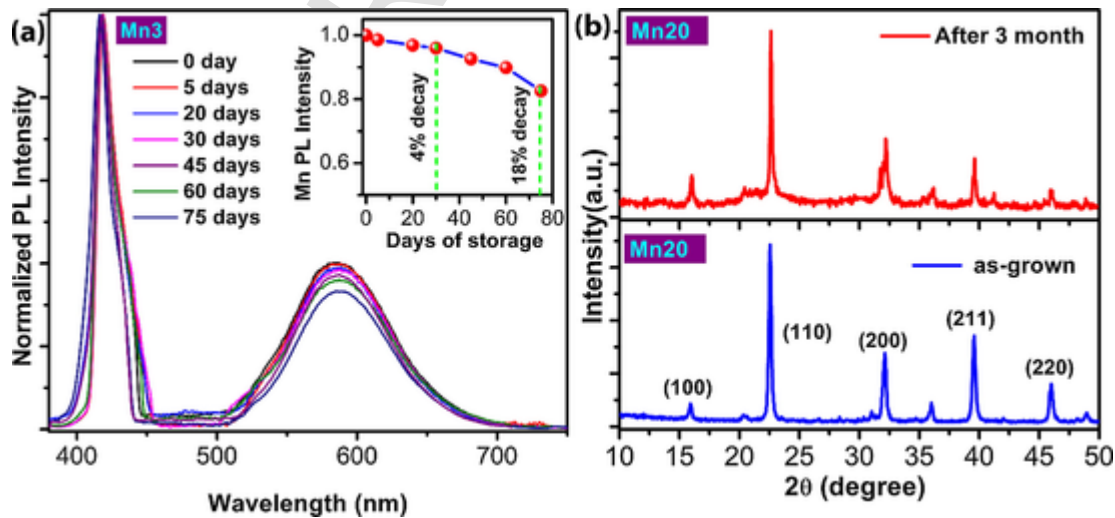


Fig. 7. Stability of the Mn doped perovskite NCs: (a) Comparison of normalized PL spectra of Mn3 at different time intervals up to 75 days stored in ambient condition after synthesis. The inset shows the variation of PL intensity (Mn related) as a function of storage time in ambient condition. It shows only 4% decay in Mn PL intensity after 30 days of storage. (b) Comparison of XRD pattern of as-grown Mn20 and after 5 months of storage of Mn20.

hot injection method, Mn ions are adsorbed and doped near the surface of the NCs. Thus, the Mn related emission usually quenches very fast as Mn diffuses out of the NCs. Chen et al. reported >50% quenching of Mn related PL emission with respect to excitonic PL intensity after 30 days of storage [45]. In contrast, we observed only 4% quenching in PL intensity after 30 days of storage, and only 18% quenching (relative to the excitonic peak intensity) after 75 days of storage, as shown in Fig. 7(a). Thus, the stability of our doped samples is much superior to those reported in the literature. Note that both the excitonic and orange-red PL peak intensities were decreased with the storage time. Due to the very high pressure-mediated synthesis conditions and lattice strain induced in physical milling process, high Mn doping efficiencies are achieved throughout the CsPbCl<sub>3</sub> host NCs. Thus, synthesis by physical milling possibly provides more efficient transfer of energy than other synthesis methods to achieve higher Mn substitution and stronger bonding in the CsPbCl<sub>3</sub> host lattice. Note that stability of our Mn doped NCs also much superior than other metal doped CsPbCl<sub>3</sub> NCs [46]. Fig. 7(b) shows the comparison of the XRD pattern of as-grown

Mn20 and that after 3 month of storage. The XRD peaks are unchanged and thus the structural stability of the doped NCs after 3 months of storage is evident from the data. Thus, our results demonstrate the room temperature solid-state synthesis of Mn-doped CsPbCl<sub>3</sub> NCs with much superior ambient stability.

### 3.8. Application of Mn doped NCs in the WLEDs

We further demonstrate the great potential of orange-red emitting Mn-doped CsPbCl<sub>3</sub> NCs for lighting and display applications. As Mn-doped CsPbCl<sub>3</sub> NCs exhibit bright orange-red emission, for the white light emission, blue and green light-emitting materials are also required. For the construction of the white LED (WLED), we further synthesized two more highly luminescent all-inorganic perovskite NCs by the same physical milling method. CsPbBr<sub>3</sub> NCs produce very bright green emission while CsPbCl<sub>1.5</sub>Br<sub>1.5</sub> NCs give bright blue emission. Fig. 8(a) shows the FETEM image of as-synthesized CsPbBr<sub>3</sub> NCs, while Fig. 8(b) shows the HRTEM lattice fringe of single CsPbBr<sub>3</sub>

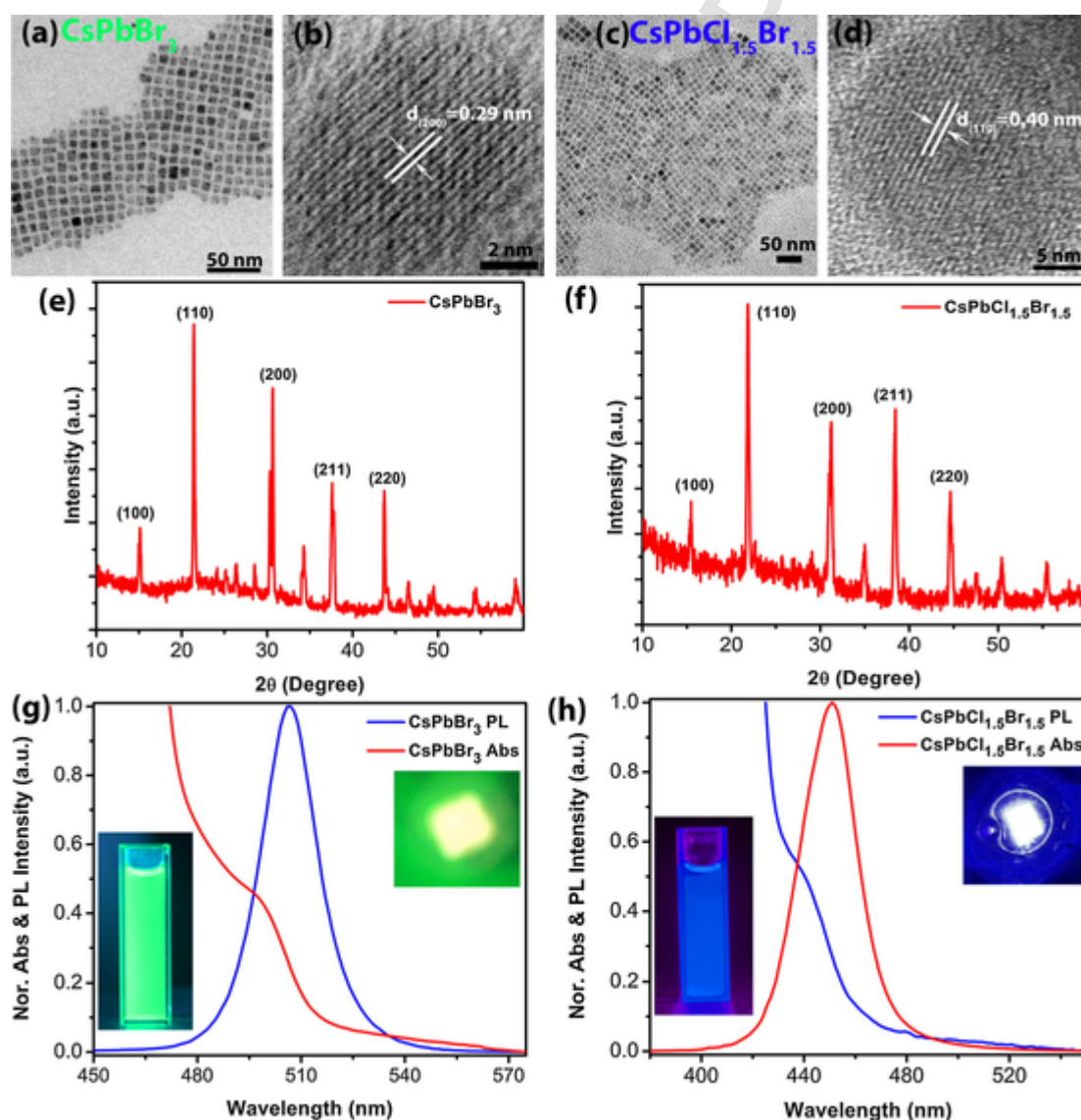


**Fig. 8.** (a) FETEM image of CsPbBr<sub>3</sub> NCs and (b) the corresponding HRTEM lattice fringe image. (c) FETEM image of CsPbCl<sub>1.5</sub>Br<sub>1.5</sub> NC and (d) the corresponding HRTEM lattice fringe image. (e, f) XRD pattern of CsPbBr<sub>3</sub> and CsPbCl<sub>1.5</sub>Br<sub>1.5</sub> NCs. (g) Normalized PL and absorption spectra of CsPbBr<sub>3</sub> NCs. The left inset shows the digital photograph of CsPbBr<sub>3</sub> NCs under UV light illumination. Right inset depicts the photograph of UV LED chip coated with CsPbBr<sub>3</sub> NCs/PMMA composite. (h) Normalized PL and absorption spectra of CsPbCl<sub>1.5</sub>Br<sub>1.5</sub> NCs. Left inset shows the digital photograph of CsPbCl<sub>1.5</sub>Br<sub>1.5</sub> NCs under UV light illumination. Right inset depicts the photograph of white light emitted from CsPbCl<sub>1.5</sub>Br<sub>1.5</sub> NCs/PMMA composite.

NC. The lattice spacing of 0.29 nm corresponds to the (2 0 0) lattice plane of CsPbBr<sub>3</sub>. Fig. 8(c) shows the FETEM image of as-grown CsPbCl<sub>1.5</sub>Br<sub>1.5</sub> NCs, while Fig. 8(d) exhibits the HRTEM lattice fringe of single CsPbCl<sub>1.5</sub>Br<sub>1.5</sub> NC. The lattice spacing of 0.40 nm corresponds to the (1 1 0) lattice plane of CsPbCl<sub>1.5</sub>Br<sub>1.5</sub>. The XRD pattern of CsPbBr<sub>3</sub> is shown in Fig. 8(e), whereas (f) shows the XRD pattern of CsPbCl<sub>1.5</sub>Br<sub>1.5</sub>. The XRD patterns confirm the proper crystalline phase of the NCs. Fig. 8(g) depicts the normalized absorbance and PL spectra CsPbBr<sub>3</sub> NCs dispersed in toluene. The left inset shows the bright green emission of the NCs under UV light, while the right inset shows a UV LED chip coated with CsPbBr<sub>3</sub> NCs/PMMA composite exhibiting the green emission. The normalized absorbance and emission spectra CsPbCl<sub>1.5</sub>Br<sub>1.5</sub> NCs are shown in Fig. 8(h). The left inset shows the bright blue emission of the NCs under UV light irradiation and the right inset shows a UV LED chip coated with CsPbCl<sub>1.5</sub>Br<sub>1.5</sub> NCs/PMMA composite showing the blue emission. The PL QY of CsPbBr<sub>3</sub> NCs and CsPbCl<sub>1.5</sub>Br<sub>1.5</sub> NCs were obtained to be 88.1% and 19.7%, respectively, which are very significant.

Note that the undoped CsPbBr<sub>3</sub>, CsPbCl<sub>1.5</sub>Br<sub>1.5</sub>, and Mn-doped CsPbCl<sub>3</sub> all the three NCs have the high absorbance in the UV region. Thus, blue, green and orange-red all the three emissions can be observed simultaneously by UV light excitation. A prototype white light-emitting device was designed by coupling a low cost and commercially available 396 nm UV chip with blue-emitting CsPbCl<sub>1.5</sub>Br<sub>1.5</sub>/PMMA film, green-emitting CsPbBr<sub>3</sub>/PMMA film and orange-red emitting 10% Mn-doped CsPbCl<sub>3</sub>/PMMA film vertically stacked together. The electroluminescence (EL) spectrum of the device is shown in Fig. 9(a), while schematic of the WLED device is depicted in the inset of Fig. 9(a) [37,33]. The coupled CsPbCl<sub>1.5</sub>Br<sub>1.5</sub>/CsPbBr<sub>3</sub>/10% Mn-doped CsPbCl<sub>3</sub> film with UV chip yields blue-green-orange tri-color emissions leading to bright pure white light emission with corresponding CIE color coordinates of (0.31, 0.34), as shown in Fig. 9(b). Thus, the CIE color coordinates lie very close to that of the pure white light (0.33, 0.33) [37,47]. Therefore our results indicate that the orange-red emitting Mn-doped CsPbCl<sub>3</sub> is significantly beneficial for obtaining white light. The optoelectronic performance of the constructed WLEDs with NCs synthesis by physical milling may be further improved by optimizing the thickness of different layers and device structure geometry.

#### 4. Conclusions

We presented a facile, low-cost, bulk scale, room temperature solid-state synthesis of highly luminescent Mn-doped CsPbCl<sub>3</sub> NCs with high Mn substitution through a physical milling method, for the first time. Perovskite NCs of sizes 9–14 nm with excellent optical properties and superior stability were achieved. The structural analysis by XRD and XPS confirm the successful doping of Mn in CsPbCl<sub>3</sub> NCs by substitution of Pb with Mn ions. We demonstrated the tunability of the Mn-re-

lated orange-red PL emission intensity by controlling the doping concentration, excitation intensity, and measurement temperature. The low-temperature PL and excitation intensity-dependent PL study reveals important insights into the origin and color tunability of Mn related orange-red PL in the dual color emitting Mn-doped CsPbCl<sub>3</sub> NCs. Importantly, it is demonstrated that Mn-doped CsPbCl<sub>3</sub> NCs synthesized by the physical milling method exhibit better emission stability over a long time due to the high Mn doping efficiencies achieved through the non-equilibrium process of synthesis. Deconvolution of the PL spectra revealed the contribution of the defect-related emission, besides the excitonic emission and Mn related emission in the overall PL spectra. Further, white LED device was demonstrated by employing blue-emitting CsPbCl<sub>1.5</sub>Br<sub>1.5</sub> NCs, green-emitting CsPbBr<sub>3</sub> NCs and orange-red emitting 10% Mn-doped CsPbCl<sub>3</sub> NCs composite films with PMMA. All NCs were synthesized by the same solid-state process. Thus, our work demonstrates a low-cost room temperature synthesis strategy of Mn-doped CsPbCl<sub>3</sub> NCs with high color tunability and superior ambient stability for white light-emitting applications. Our report may stimulate further investigation of novel low-cost solid-state synthesis of perovskite NCs and quantum dots for cutting-edge optoelectronic applications.

#### CRedit authorship contribution statement

**Joydip Ghosh:** Conceptualization, Methodology, Formal analysis, Writing - original draft. **Modasser Hossain:** Methodology, Formal analysis. **P.K. Giri:** Conceptualization, Formal analysis, Validation, Writing - review & editing, Supervision, Funding acquisition.

#### Declaration of Competing Interest

The authors declare that they have no known competing financial interests or personal relationships that could have appeared to influence the work reported in this paper.

#### Acknowledgment

We acknowledge the financial support from MEITY (Grant No. 5(9)/2012-NANO(VOL-II)) for carrying out part of this work. Central Instruments Facility, IIT Guwahati is acknowledged for the FETEM and TRPL facilities. We gratefully acknowledge the support provided by Dr. H. Sugimoto and Prof. M. Fujii, Kobe University for the XPS measurement.

#### Appendix A. Supplementary material

Supplementary data to this article can be found online at <https://doi.org/10.1016/j.jcis.2019.12.066>.

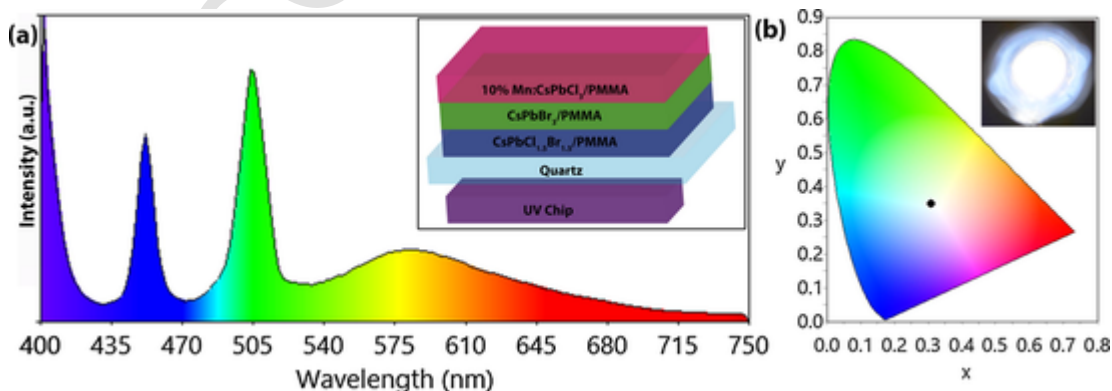


Fig. 9. (a) EL emission spectrum of 10% Mn-doped CsPbCl<sub>3</sub>/CsPbBr<sub>3</sub>/CsPbCl<sub>1.5</sub>Br<sub>1.5</sub> NCs film with PMMA on a UV LED chip. The inset shows a schematic of the device structure of WLED. (b) Chromaticity diagram showing the CIE coordinates of the WLED. Inset shows the digital photograph of the constructed WLED.

## References

- [1] L.N. Quan, B.P. Rand, R.H. Friend, S.G. Mhaisalkar, T.-W. Lee, E.H. Sargent, Perovskites for next-generation optical sources, *Chem. Rev.* 119 (12) (2019) 7444–7477.
- [2] K. Lin, J. Xing, L.N. Quan, F.P.G. de Arquer, X. Gong, J. Lu, L. Xie, W. Zhao, D. Zhang, C. Yan, W. Li, X. Liu, Y. Lu, J. Kirman, E.H. Sargent, Q. Xiong, Z. Wei, Perovskite light-emitting diodes with external quantum efficiency exceeding 20 per cent, *Nature* 562 (7726) (2018) 245–248.
- [3] S.I. Seok, M. Grätzel, N.-G. Park, Methodologies toward highly efficient perovskite solar cells, *Small* 14 (20) (2018) 1704177.
- [4] J.-P. Correa-Baena, A. Abate, M. Saliba, W. Tress, T. Jesper Jacobsson, M. Grätzel, A. Hagfeldt, The rapid evolution of highly efficient perovskite solar cells, *Energy Environ. Sci.* 10 (3) (2017) 710–727.
- [5] L. Protesescu, S. Yakunin, M.I. Bodnarchuk, F. Krieg, R. Caputo, C.H. Hendon, R.X. Yang, A. Walsh, M.V. Kovalenko, Nanocrystals of cesium lead halide perovskites (CsPbX<sub>3</sub>, X = Cl, Br, and I): novel optoelectronic materials showing bright emission with wide color gamut, *Nano Lett.* 15 (6) (2015) 3692–3696.
- [6] Y.-H. Suh, T. Kim, J.W. Choi, G.-L. Lee, J. Park, High-performance CsPbX<sub>3</sub> perovskite quantum-dot light-emitting devices via solid-state ligand exchange, *ACS Appl. Nano Mater.* 1 (2) (2018) 488–496.
- [7] H. Wang, X. Zhang, Q. Wu, F. Cao, D. Yang, Y. Shang, Z. Ning, W. Zhang, W. Zheng, Y. Yan, S.V. Kershaw, L. Zhang, A.L. Rogach, X. Yang, Trifluoroacetate induced small-grained CsPbBr<sub>3</sub> perovskite films result in efficient and stable light-emitting devices, *Nat. Commun.* 10 (1) (2019) 665.
- [8] J. Zeng, X. Li, Y. Wu, D. Yang, Z. Sun, Z. Song, H. Wang, H. Zeng, Space-confined growth of CsPbBr<sub>3</sub> film achieving photodetectors with high performance in all figures of merit, *Adv. Funct. Mater.* 28 (43) (2018) 1804394.
- [9] J. Ghosh, R. Ghosh, P.K. Giri, Mesoporous Si nanowire templated controlled fabrication of organometal halide perovskite nanoparticles with high photoluminescence quantum yield for light-emitting applications, *ACS Appl. Nano Mater.* 1 (4) (2018) 1551–1562.
- [10] J. Ghosh, G. Natu, P.K. Giri, Plasmonic hole-transport-layer enabled self-powered hybrid perovskite photodetector using a modified perovskite deposition method in ambient air, *Org. Electron.* 71 (2019) 175–184.
- [11] L. Yang, A.T. Barrows, D.G. Lidzey, T. Wang, Recent progress and challenges of organometal halide perovskite solar cells, *Rep. Prog. Phys.* 79 (2) (2016) 26501.
- [12] T.C. Jellicoe, J.M. Richter, H.F.J. Glass, M. Tabachnyk, R. Brady, S.E. Dutton, A. Rao, R.H. Friend, D. Credgington, N.C. Greenham, M.L. Böhm, Synthesis and optical properties of lead-free cesium tin halide perovskite nanocrystals, *J. Am. Chem. Soc.* 138 (9) (2016) 2941–2944.
- [13] H. Liu, Z. Wu, J. Shao, D. Yao, H. Gao, Y. Liu, W. Yu, H. Zhang, B. Yang, CsPb<sub>1-x</sub>Mn<sub>x</sub>Cl<sub>3</sub> perovskite quantum dots with high Mn substitution ratio, *ACS Nano* 11 (2) (2017) 2239–2247.
- [14] S. Das Adhikari, S.K. Dutta, A. Dutta, A.K. Guria, N. Pradhan, Chemically tailoring the dopant emission in manganese-doped CsPbCl<sub>3</sub> perovskite nanocrystals, *Angew. Chem. Int. Ed.* 56 (30) (2017) 8746–8750.
- [15] S. Das Adhikari, R.K. Behera, S. Bera, N. Pradhan, Presence of metal chloride for minimizing the halide deficiency and maximizing the doping efficiency in Mn(II)-doped CsPbCl<sub>3</sub> nanocrystals, *J. Phys. Chem. Lett.* 10 (7) (2019) 1530–1536.
- [16] X. Yuan, S. Ji, M.C. De Siena, L. Fei, Z. Zhao, Y. Wang, H. Li, J. Zhao, D.R. Gamelin, Photoluminescence temperature dependence, dynamics, and quantum efficiencies in Mn<sup>2+</sup>-doped CsPbCl<sub>3</sub> perovskite nanocrystals with varied dopant concentration, *Chem. Mater.* 29 (18) (2017) 8003–8011.
- [17] D. Rossi, D. Parobek, Y. Dong, D.H. Son, Dynamics of exciton–Mn energy transfer in Mn-doped CsPbCl<sub>3</sub> perovskite nanocrystals, *J. Phys. Chem. C* 121 (32) (2017) 17143–17149.
- [18] C.C. Lin, K.Y. Xu, D. Wang, A. Meijerink, Luminescent manganese-doped CsPbCl<sub>3</sub> perovskite quantum dots, *Sci. Rep.* 7 (2017) 45906.
- [19] Y. Zhou, J. Chen, O.M. Bakr, H.-T. Sun, Metal-doped lead halide perovskites: synthesis, properties, and optoelectronic applications, *Chem. Mater.* 30 (19) (2018) 6589–6613.
- [20] D. Parobek, B.J. Roman, Y. Dong, H. Jin, E. Lee, M. Sheldon, D.H. Son, Exciton-to-dopant energy transfer in Mn-doped cesium lead halide perovskite nanocrystals, *Nano Lett.* 16 (12) (2016) 7376–7380.
- [21] J. Zhu, X. Yang, Y. Zhu, Y. Wang, J. Cai, J. Shen, L. Sun, C. Li, Room-temperature synthesis of Mn-doped cesium lead halide quantum dots with high Mn substitution ratio, *J. Phys. Chem. Lett.* 8 (17) (2017) 4167–4171.
- [22] A. De, N. Mondal, A. Samanta, Luminescence tuning and exciton dynamics of Mn-doped CsPbCl<sub>3</sub> nanocrystals, *Nanoscale* 9 (43) (2017) 16722–16727.
- [23] D. Chen, S. Zhou, G. Fang, X. Chen, J. Zhong, Fast room-temperature cation exchange synthesis of Mn-doped CsPbCl<sub>3</sub> nanocrystals driven by dynamic halogen exchange, *ACS Appl. Mater. Interfaces* 10 (46) (2018) 39872–39878.
- [24] W. Chen, T. Shi, J. Du, Z. Zang, Z. Yao, M. Li, K. Sun, W. Hu, Y. Leng, X. Tang, Highly stable silica-wrapped Mn-doped CsPbCl<sub>3</sub> quantum dots for bright white light-emitting devices, *ACS Appl. Mater. Interfaces* 10 (50) (2018) 43978–43986.
- [25] Z.-Y. Zhu, Q.-Q. Yang, L.-F. Gao, L. Zhang, A.-Y. Shi, C.-L. Sun, Q. Wang, H.-L. Zhang, Solvent-free mechanosynthesis of composition-tunable cesium lead halide perovskite quantum dots, *J. Phys. Chem. Lett.* 8 (7) (2017) 1610–1614.
- [26] W. Wu, W. Liu, Q. Wang, Q. Han, Q. Yang, Temperature-dependent photoluminescence of pure and Mn-doped CsPbCl<sub>3</sub> nanocrystals, *J. Alloy. Compd.* 787 (2019) 165–172.
- [27] G. Kaupp, Solid-state molecular syntheses: complete reactions without auxiliaries based on the new solid-state mechanism, *CrystEngComm* 5 (23) (2003) 117–133.
- [28] T. Friščić, I. Halasz, P.J. Beldon, A.M. Belenguer, F. Adams, S.A.J. Kimber, V. Honkimäki, R.E. Dinnebier, Real-time and in situ monitoring of mechanochemical milling reactions, *Nat. Chem.* 5 (2012) 66.
- [29] J. Zhu, F. Liu, G.B. Stringfellow, S.-H. Wei, Strain-enhanced doping in semiconductors: effects of dopant size and charge state, *Phys. Rev. Lett.* 105 (19) (2010) 195503.
- [30] W. Liu, J. Zheng, S. Cao, L. Wang, F. Gao, K.-C. Chou, X. Hou, W. Yang, Mass production of Mn<sup>2+</sup>-doped CsPbCl<sub>3</sub> perovskite nanocrystals with high quality and enhanced optical performance, *Inorg. Chem. Front.* 5 (10) (2018) 2641–2647.
- [31] W.J. Mir, M. Jagadeeswararao, S. Das, A. Nag, Colloidal Mn-doped cesium lead halide perovskite nanoplatelets, *ACS Energy Lett.* 2 (3) (2017) 537–543.
- [32] Y. Liu, G. Pan, R. Wang, H. Shao, H. Wang, W. Xu, H. Cui, H. Song, Considerably enhanced exciton emission of CsPbCl<sub>3</sub> perovskite quantum dots by the introduction of potassium and lanthanide ions, *Nanoscale* 10 (29) (2018) 14067–14072.
- [33] M. He, Y. Cheng, L. Shen, C. Shen, H. Zhang, W. Xiang, X. Liang, Mn-doped CsPbCl<sub>3</sub> perovskite quantum dots (PQDs) incorporated into silica/alumina particles used for WLEDs, *Appl. Surf. Sci.* 448 (2018) 400–406.
- [34] J. Ghosh, R. Ghosh, P.K. Giri, Tuning the visible photoluminescence in Al doped ZnO thin film and its application in label-free glucose detection, *Sens. Actuators, B* 254 (2018) 681–689.
- [35] Z.-J. Li, E. Hofman, A.H. Davis, A. Khamrang, J.T. Wright, B. Dzikovski, R.W. Meulenbergh, W. Zheng, Complete dopant substitution by spinodal decomposition in Mn-doped two-dimensional CsPbCl<sub>3</sub> nanoplatelets, *Chem. Mater.* 30 (18) (2018) 6400–6409.
- [36] O. Chen, D.E. Shelby, Y. Yang, J. Zhuang, T. Wang, C. Niu, N. Omenetto, Y.C. Cao, Excitation-intensity-dependent color-tunable dual emissions from manganese-doped CdS/ZnS core/shell nanocrystals, *Angew. Chem.* 122 (52) (2010) 10330–10333.
- [37] S. Ye, J.-Y. Sun, Y.-H. Han, Y.-Y. Zhou, Q.-Y. Zhang, Confining Mn<sup>2+</sup>-doped lead halide perovskite in zeolite-Y as ultrastable orange-red phosphor composites for white light-emitting diodes, *ACS Appl. Mater. Interfaces* 10 (29) (2018) 24656–24664.
- [38] S. Zou, Y. Liu, J. Li, C. Liu, R. Feng, F. Jiang, Y. Li, J. Song, H. Zeng, M. Hong, X. Chen, Stabilizing cesium lead halide perovskite lattice through Mn(II) substitution for air-stable light-emitting diodes, *J. Am. Chem. Soc.* 139 (33) (2017) 11443–11450.
- [39] J. Ghosh, R. Ghosh, P.K. Giri, Strong cathodoluminescence and fast photore-sponse from embedded CH<sub>3</sub>NH<sub>3</sub>PbBr<sub>3</sub> nanoparticles exhibiting high ambient stability, *ACS Appl. Mater. Interfaces* 11 (16) (2019) 14917–14931.
- [40] X. Yuan, J. Zheng, R. Zeng, P. Jing, W. Ji, J. Zhao, W. Yang, H. Li, Thermal stability of Mn<sup>2+</sup> ion luminescence in Mn-doped core-shell quantum dots, *Nanoscale* 6 (1) (2014) 300–307.
- [41] S. Parveen, K.K. Paul, R. Das, P.K. Giri, Large exciton binding energy, high photoluminescence quantum yield and improved photostability of organo-metal halide hybrid perovskite quantum dots grown on a mesoporous titanium dioxide template, *J. Colloid Interface Sci.* 539 (2019) 619–633.
- [42] A.A. Lohar, A. Shinde, R. Gahlaut, A. Sagdeo, S. Mahamuni, Enhanced photoluminescence and stimulated emission in CsPbCl<sub>3</sub> nanocrystals at low temperature, *J. Phys. Chem. C* 122 (43) (2018) 25014–25020.
- [43] C. Carabatos-Nédelec, M. Oussaid, K. Nitsch, Raman scattering investigation of cesium plumbochloride, CsPbCl<sub>3</sub>, phase transitions, *J. Raman Spectrosc.* 34 (5) (2003) 388–393.
- [44] J. Singh, *Semiconductor Devices: An Introduction*.
- [45] D. Chen, G. Fang, X. Chen, L. Lei, J. Zhong, Q. Mao, S. Zhou, J. Li, Mn-doped CsPbCl<sub>3</sub> perovskite nanocrystals: solvothermal synthesis, dual-color luminescence and improved stability, *J. Mater. Chem. C* 6 (33) (2018) 8990–8998.
- [46] P.J.S. Rana, T. Swetha, H. Mandal, A. Saeki, P.R. Bangal, S.P. Singh, Energy transfer dynamics of highly stable Fe<sup>3+</sup>-doped CsPbCl<sub>3</sub> perovskite nanocrystals with dual-color emission, *J. Phys. Chem. C* 123 (27) (2019) 17026–17034.
- [47] R. Ghosh, J. Ghosh, R. Das, L.P.L. Mawlong, K.K. Paul, P.K. Giri, Multifunctional Ag nanoparticle decorated Si nanowires for sensing, photocatalysis and light emission applications, *J. Colloid Interface Sci.* 532 (2018) 464–473.